Understanding the fast phase-change mechanism of tetrahedrally bonded Cu_2GeTe_3: Comprehensive analyses of electronic structure and transport phenomena

Keisuke Kobayashi,[1,2,*] Jonathan M. Skelton,[3,4] Yuta Saito,[5] Satoshi Shindo,[6] Masaaki Kobata,[7] Paul Fons,[5] Alexander V. Kolobov,[5] Stephen Elliott,[3] Daisuke Ando,[6] and Yuji Sutou[6,†]

[1]*Materials Sciences Research Center, Japan Atomic Energy Agency, 1-1-1 Kouto, Sayo-cho, Hyogo, 679-5148, Japan*

[2]*Research Institute of KUT, Kouchi University of Technology, Tosa yamada, Kami City, Kochi 782-8502, Japan*

[3]*Department of Chemistry, University of Cambridge, Cambridge CB2 1EW, United Kingdom*

[4]*Department of Chemistry, University of Bath, Claverton Down, United Kingdom*

[5]*Nanoelectronics Research Institute, National Institute of Advanced Industrial Science and Technology, Tsukuba Central 5, Higashi 1-1-1, Tsukuba, Ibaraki, 305-8565, Japan*

[6]*Department of Materials Science, Graduate School of Engineering, Tohoku University, 6-6-11 Aoba-yama, Sendai 980-8579, Japan*

[7]*Collaborative Laboratories for Advanced Decommissioning Science, Japan Atomic Energy Agency, 2-4 Shirakata, Tokai-mura, Naka-gun, Ibaraki 319-1195, Japan*

(Received 7 November 2017; revised manuscript received 15 March 2018; published 3 May 2018)

Cu_2GeTe_3 (CGT) phase-change material, a promising candidate for advanced fast nonvolatile random-access-memory devices, has a chalcopyritelike structure with sp^3 bonding in the crystalline phase; thus, the phase-change (PC) mechanism is considered to be essentially different from that of the standard PC materials (e.g., Ge-Sb-Te) with threefold to sixfold p-like bonding. In order to reveal the PC mechanism of CGT, the electronic structure change due to PC has been investigated by laboratory hard x-ray photoelectron spectroscopy and combined first-principles density-functional theory molecular-dynamics simulations. The valence-band spectra, in both crystalline and amorphous phases, are well simulated by the calculations. An inherent tendency of Te 5s lone-pair formation and an enhanced participation of Cu 3d orbitals in the bonding are found to play dominant roles in the PC mechanism. The electrical conductivity of as-deposited films and its change during the PC process is investigated in connection with valence-band spectral changes near the Fermi level. The results are successfully analyzed, based on a model proposed by Davis and Mott for chalcogenide amorphous semiconductors. The results suggest that robustness of the defect-band states against thermal stress is a key to the practical application of this material for memory devices.

DOI: 10.1103/PhysRevB.97.195105

I. INTRODUCTION

The functionality of phase-change materials (PCMs), which exhibit rapid and reversible switching between amorphous and metastable crystalline phases, is widely used for the storage of binary information [1–4]. In optical digital storage devices, such as DVD and Blu-ray Discs, information is encoded via the material structure using changes in the optical reflectivity between the amorphous and crystalline phases [5,6]. The electrical-resistance contrast between the two phases is harnessed in phase-change random-access memory (PCRAM) devices, which are competing with other devices such as magnetoresistive RAM (MRAM), ferroelectric RAM (FeRAM), and resistive RAM (ReRAM), to replace Si-based nonvolatile flash technology [7].

Sutou *et al.* have reported that the ternary alloy, Cu_2GeTe_3 (CGT), holds much promise as a new type of PCM [8–10]. CGT has been shown to possess several favorable characteristics for fast rewritable memory devices over standard PCMs fabricated from GeTe-Sb_2Te_3 (GST) pseudobinary PCM alloys, due to its relatively short crystallization time [10], long-term data-retention properties, and reduced amorphization power requirements [9]. Anomalously, the density of amorphous CGT (a-CGT) is higher than that of crystalline CGT (c-CGT) by about 2-4%, a property contrast opposite to that of GST alloys, which show a corresponding density increase of ∼6.5% on crystallization. This suggests the possibility of enhanced device-cycling endurance for CGT-based devices, since large density changes, regardless of sign, can lead to mechanical stresses and delamination within device structures and, ultimately, to device failure [9,10]. Furthermore, a zero density change upon crystallization was achieved for the Cu-Ge-Te ternary system for alloys along the GeTe-Cu_2GeTe_3 pseudobinary line [11]. On the other hand, optical-reflectivity changes correlate with changes in density and are described by the Clausius-Mossotti relation; this effect is thus smaller than in GST upon PC; and therefore less preferable for optical-memory applications [9–11].

The most interesting feature of CGT is that it has 24 s-p electrons per formula unit (i.e., 4 s-p electrons per atom) and thus can undergo sp^3 hybridization and tetrahedral bonding. As has been well established, an essential feature of the prototypical PCMs GST and AIST (e.g., $Ag_{3.5}In_{3.8}Sb_{75.0}Te_{17.7}$) and their related compounds, is that these alloys exhibit defective octahedral bonding coordination in the crystalline

*koba_kei@spring8.or.jp
†ysutou@material.tohoku.ac.jp

phase due to their unusual valence-electron configuration. Both GST and AIST alloys are regarded as belonging to the average-5 valence-electron family ($\langle V \rangle$), with bonds being sustained by half-filled resonance bonding with p_x, p_y, and p_z orbitals [12–18]. The total of six equivalent half-filled bonds between cations and anions tend to split into three long and three short bonds to reduce the electronic part of the free energy, at the expense of an elastic-energy increase. This tradeoff takes place randomly throughout the whole material structure. The phase change into the amorphous state is characterized by a collapse of the coherent octahedral bonding into a disordered local bonding network, which is approximately consistent with the Mott 8-N rule in appearance. In spite of the band gap widening, the whole electronic structure remains largely unchanged (except in the proximity of the valence-band top) because the bonding character is still predominantly p-like in the amorphous phase [18–20]. In contrast, CGT has four s-p electrons/atom and adopts a chalcopyritelike structure with a tetrahedral sp^3 bonding network [21]. As sp^3 tetrahedral bonding is known generally to be very rigid, materials with tetrahedral bonding have not previously been considered to be candidates for reversible PC materials. Hence, the mechanism of the reversible PC in CGT is of fundamental interest.

To provide insight into this important question, we have investigated the electronic structure and chemical bonding in CGT by means of temperature-dependent thin-film resistance/conductance measurements, bulk-sensitive hard x-ray photoelectron spectroscopy (HXPES or HAXPES) [22–24] using a laboratory Cr K_α (5.4 keV) monochromatic source for excitation [25,26], and first-principles density-functional calculations to clarify the problem [27].

II. EXPERIMENTAL DETAILS

The samples were prepared by radio-frequency (RF) magnetron sputtering using GeTe and CuTe alloy targets. Thin films of CGT were deposited on single-crystal Si wafers covered with thermal-SiO_2 layers to a film thickness of 200 nm. The growth was carried out at room temperature to obtain an amorphous film. The incorporation of the sputtering gas, Ar, is negligibly small. The stoichiometry of the samples was controlled by optimizing the sputter power ratio of each alloy target. The composition of the film was examined by inductively coupled plasma mass spectroscopy (ICP-MS), confirming that the deviation from stoichiometry was less than 10% for all elements and that the batch-to-batch compositional difference were negligibly small and within experimental error (estimated within 0.5 at.% for all elements). It was also confirmed that the composition of the film did not change after annealing for the temperature range used in this study. Electrical-resistance measurements were performed during the annealing process to monitor the crystallization process. The temperature dependence of the conductivity was also measured for as-deposited films in the temperature range between 80 and 473 K. Hall-effect measurements were carried out at room temperature on both as-deposited amorphous and annealed crystalline samples. The microstructure of the films after crystallization was observed by a transmission electron microscope (TEM) at an acceleration voltage of 200 kV. The surfaces of the samples were capped with 3 nm carbon layers soon after the film growth to protect against oxidation [18,28]. Due to the small photoionization cross section of carbon, the capping layers did not lead to any apparent modification of the recorded HXPES spectra. The laboratory HXPES measurements were performed at a laboratory at SPring-8 using the HEARP Lab system [25,26], which consists of a Cr K_α source with a Ge422 Rowland monochromator, a wide-acceptance objective lens, and an R4000 10 kV VG Scienta analyzer. The total energy resolution was estimated to be 0.55 eV. In order to investigate changes in the valence-band spectra in the vicinity of the Fermi level precisely, we have also performed valence-band HXPES measurements on BL47XU at SPring-8. The excitation photon energy was 8 keV, and the total energy resolution was 0.25 eV in these measurements.

Density-functional theory (DFT) electronic-structure calculations were carried out within the pseudopotential plane-wave formalism, as implemented in the Vienna *ab initio* simulation package (VASP) code [27]. The starting point for the calculations was an optimized 96-atom $2 \times 2 \times 2$ supercell expansion of the chalcopyrite crystalline CGT structure and 96-atom melt-quenched amorphous model from our previous modeling study [29]. Electronic-structure calculations were performed on these models using the PBE0 hybrid exchange-correlation functional [30]. Projector augmented-wave (PAW) pseudopotentials [31] were used to model the core electrons, with the Cu 4s and 3d, Ge 4s and 4p, and Te 5s and 5p electrons being treated as valence electrons. The kinetic energy of the plane-wave basis was set to 369.3 eV. Uniform Γ-centered Monkhorst-Pack k-point meshes [32] with $1 \times 3 \times 2$ and $2 \times 2 \times 2$ subdivisions were used to sample the electronic Brillouin zones of the crystalline and amorphous models, respectively, and a Gaussian smearing with a width of 0.1 eV was applied during the Brillouin-zone integration. We note that, unlike in the calculations in Ref. [32], the Cu and Ge semicore electrons were treated as core states, and we did not perform spin-polarized calculations. The former allowed for a reduction in the plane-wave cutoff. Careful testing revealed that these simplifications had a negligible effect on the structure of the valence- and conduction-band densities of states (DOS) in the vicinity of the Fermi energy, as is relevant to the present work, and omitting them considerably reduced the computational cost of the hybrid calculations.

III. RESULTS AND DISCUSSION

Figure 1(a) shows the temperature dependence of the sample electrical resistance during annealing and on subsequent cooling. The sample films were prepared by sputtering in the same batch, and cut into pieces. Then, the resistance of each sample was measured as a function of temperature during raising the temperature up to different temperatures between 230 and 400 °C, and then cooling down to room temperature. When the annealing temperature exceeded ∼230 °C, the sample resistance began to rapidly decrease, concomitant with the onset of crystallization [9]. The fluctuation of the resistance at around 200 °C is thought to be due to surface oxidation of the samples despite the 3 nm thick carbon cap intended to prevent this [28]. Since the surface oxide is very thin (on the order of a few nm), and HXPES is a bulk-sensitive technique, the

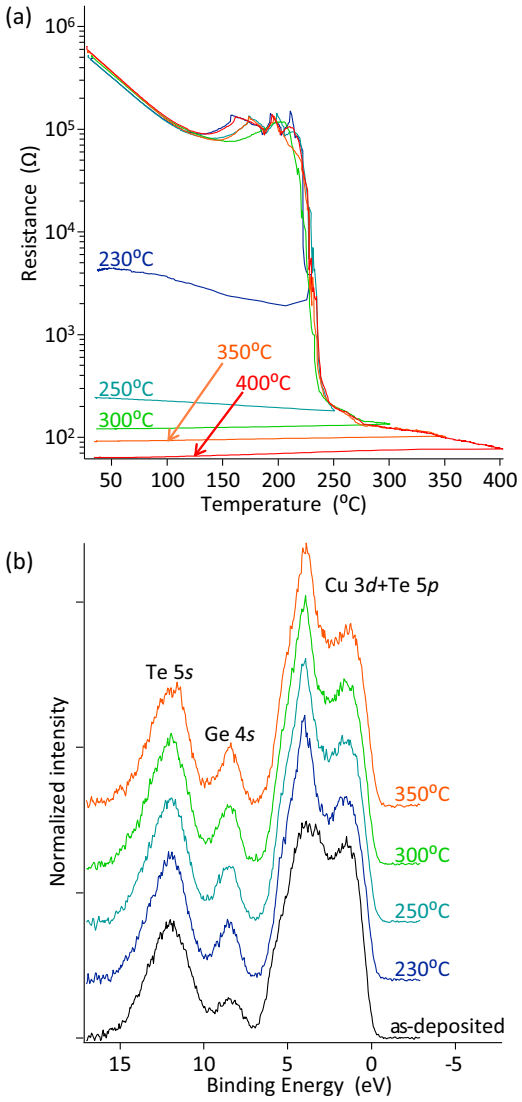

FIG. 1. (a) Film resistance variations during heating-cooling cycles of CGT. Different films were used for different cycles, where a two-point probe method was used for the measurement. The maximum temperature of each cycle is denoted in the figure. (b) Annealing temperature dependence of the valence-band spectral shape.

effect of oxidation on the valence-band spectra is expected to be negligible. The slope of the resistance versus temperature curve decreases when the annealing temperature reaches ∼250 °C. Its sign changes from being negative to positive at a temperature between 250 °C and 300 °C, as shown in Fig. 1(a). It was found by Hall-effect measurements that the Hall mobilities of the amorphous and crystalline phases are about 0.2 and 5.0 $cm^2/V\,s$, respectively, and the carrier concentrations of the amorphous and crystalline phases are about 6.6×10^{18} cm^{-3} and 3.2×10^{21} cm^{-3}, respectively. There is a three-order difference in carrier concentration between the two phases and more than a one-order difference in the mobility that is consistent with the four-order difference in total resistance change seen upon crystallization. It also should be noted that the resistivity (conductivity) of both the amorphous and crystalline phases of CGT are lower (higher) than that of GST a trend that is consistent with a previous study reporting a direct comparison of resistance measurements [9]. A comparison of resistance behavior during annealing-cooling procedure for GST and CGT is shown in Fig. S1 in the Supplemental Material [33].

The corresponding HXPES valence-band spectra of the as-deposited and annealed samples taken from the same batch of samples used in the resistance measurements are shown in Fig. 1(b). Based upon the *ab initio* results, the band in the region 0–6 eV is assigned to mainly Te 5*p* and Cu 3*d* states, while the peaks near 8.5 eV and 12 eV originate mainly from Ge 4*s* and Te 5*s* states, respectively. The overall spectral features do not drastically change upon crystallization; however, the Cu 3*d* feature, which peaks at around 4 eV, becomes taller, while the Ge 4*s* band becomes narrower for annealing temperatures greater than 230 °C. This temperature corresponds to the onset of the rapid resistance decrease region, as illustrated in Fig. 1(a).

A comparison of experimental (black solid curve) and simulated (red solid curve) valence-band spectra for a *c*-CGT film is shown in Fig. 2(a). The simulated spectra were obtained as weighted sums of the calculated orbital-projected partial densities of states for each atom, which were convolved with a Gaussian function with a width 0.5 eV to account for the instrumental resolution. No other broadening was involved in the simulation. The fitting was performed by minimizing the quantity $\Delta = 100\{(\Sigma[(X_i - f_i)/X_i]^2\}^{1/2}/N$, where X_i, f_i, and N are the experimental data, simulated spectral values, and the number of data points in the energy region from −15.7 eV to 0 eV with 0.05 eV steps ($N = 314$ points). The fit was very sensitive to the variation of each parameter (that is, relative cross section values). A 5% change in each parameter resulted in detectable change in Δ. In the fitting procedure, the whole calculated valence band was shifted toward lower binding by 0.7 eV in order to match the position of the top of the valence band for the crystalline phase. This necessity of a shift is due to a difference in the Fermi-level positions between the calculation (intrinsic) and experiment (extrinsic). Te *s* (15-10 eV) and Ge *s* (10-6.8 eV) bands in the calculation were needed to be additionally shifted by 0.8 and 0.4 eV towards lower binding energies, respectively. These shifts are explained to be due to the effect of an attractive potential of the final-state core holes with a localized nature of the outgoing photoelectrons [23]. In the amorphous state, no shift was necessary for the matching of calculated and experimental spectra. This is very likely to be due to broader bandwidths of the calculated features, which mask the final-state effects.

The contributions from atomic states to the simulated valence-band spectrum are shown in Fig. 2(b). The unweighted total and partial densities of states from the calculations are shown alongside a snapshot of the model in Fig. 2(e); contributions from each atomic state to the simulated spectrum in Fig. 2(b) are very different from the partial density of states in Fig. 2(e) due to weighting by the photoionization cross sections, which strongly depend on the element and orbital symmetry. Note that the double peak structure in the energy region of 0–7 eV in the *c* phase is due to Cu 3*d* originated states; however, it is due to Te *p*-like states in the *a* phase. Figures 2(c) and 2(d) provide a corresponding comparison of the experimental and simulated valence-band spectra for an *a*-CGT film, with the calculated density of states and a snapshot of the atomic configuration used in the calculation shown in Fig. 2(f).

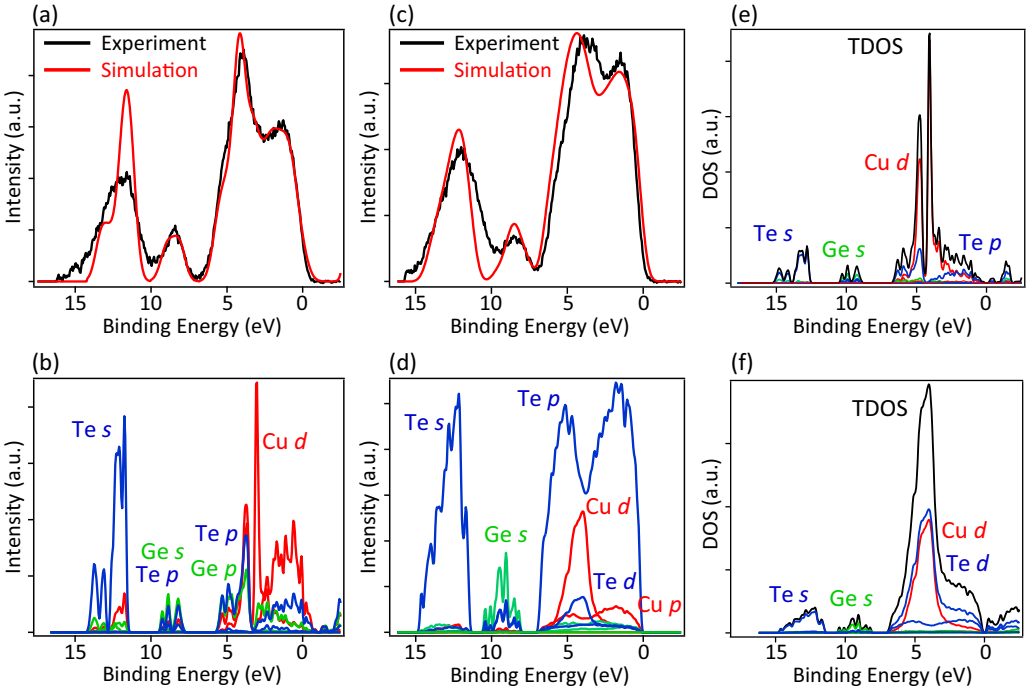

FIG. 2. Comparison of experimental (black) and simulated (red) valence-band spectra for (a) crystalline and (c) amorphous films. Contributions from the partial density of states with different orbital symmetries in the simulated spectra are shown in (b) and (d) for crystalline and amorphous films, respectively, where these spectra are weighted to take into account the photoionization cross sections. Simulated total densities of states (TDOS) and partial densities of states (PDOS) without weighting for (e) crystalline and (f) amorphous phases.

In order to verify that the present spectral simulations are reasonable, we compare the fitting parameter values for the *a* and *c* phases with theoretical values [34] in Table I. Note that the theoretical cross section for each subshell is divided by the electron occupation of the subshell in Table I. The errors involved in the parameter values in Table I are estimated to be 5% or lower, as discussed above. All the values are normalized to the values for Te *s* states. On the whole, the agreement between fitting parameters and theoretical calculations is good for both *a*-CGT and *c*-CGT, except for the anomalous deviations in Cu *p* and Te *d* states. In the *c* phase, the fitting parameter for Ge *d* states also shows an anomalously large value compared to the calculation. Based upon the results in Table I, we consider that the present fitting procedure is reasonable, and the anomalous deviations mentioned above are the results of specific chemical-bond characteristics in the *a* and *c* phases.

TABLE I. Comparison of the fitting parameter values for *a* and *c* phases of CGT with theoretical values calculated by Tzhaskovskaya *et al.* [34]. Note that the theoretical cross section for each subshell is divided by the electron occupation of the subshell. All the values are normalized to the values for the Te *s* state. As a whole, agreement between fitting parameters and theoretical calculations is good both for *a*-CGT and *c*-CGT, except for anomalous deviations for the Cu *p* and Te *d* states (in bold).

	Tzhaskovskaya	Amorphous	Crystalline
Cu *s*	0.28	0.00	0.00
Cu *p*	–	1.61	**5.53**
Cu *d*	0.17	0.10	0.24
Ge *s*	–	0.72	0.98
Ge *p*	0.74	0.72	0.98
Ge *d*	0.37	0.51	2.04
Te *s*	1.00	1.00	1.00
Te *p*	1.66	1.73	1.65
Te *d*	0.00	**0.26**	0.00

The reasonable agreement between the experimental and simulated spectra for both the *c*-CGT and *a*-CGT phases suggests that the DFT-predicted electronic structures shown in Figs. 2(e) and 2(f) can serve as a sound basis for a discussion of the electronic-structure changes occurring during PC and, at the same time, offer an insight into the reversible PC mechanism. The highest band in *c*-CGT (0–7 eV binding energy) shown in Fig. 2(e) can be separated into three sub-bands; that is, a sharp peak at 4.8 eV, which consists of contributions from Te *p* and Cu *d* states, a sharp Cu *d*-dominated peak at around 4 eV, and a broad Te *p*-Cu *d* mixed-state band extending towards the Fermi level. These features are indicative of Te *p*-Cu *d* bonding, nonbonding Cu *d*, and Te *p*-Cu *d* antibonding states, respectively. The splitting into these three bands can be naturally understood to be a result of the geometrical mismatch between the Cu 3*d* orbitals and the Te states in the tetrahedral sp^3-bonded matrix. The relative contributions to the topmost band from Cu *d*, Te *p,* and Ge *p* states are 67.3%, 22.4%, and 2.3%, respectively. The sum of the remaining contributions is 8%; however, each contribution originates from six subshells (that is the Cu *p*, Cu *s*, Ge *s*, Ge *d*. Te *s*, and Te *d* states), where each individual contribution was smaller than that of the 2.3% contribution from Ge *p* states.

The topmost band of *a*-CGT in Fig. 2(f), on the other hand, shows a striking difference from that of *c*-CGT. The two prominent sharp peaks are merged into a single broad peak centered around ∼4 eV and with a tail towards the

valence-band maximum (VBM). The Te d states make the largest contribution of 48.9% over that of Cu d states (34.8%) to this band. This dramatic increase in the participation of Te d states in the DOS may be reasonably understood to be a result of the enhanced hybridization of Te d and Cu d states, and is too prominent to be attributed to a misprojection of the plane-wave orbitals to atomiclike states. The contribution of Te and Ge p-like state contributions decrease to 11.2% and 1.5%, respectively.

Investigation of the valence-band features with the largest binding energy in Figs. 2(e) and 2(f) indicates that the contribution from Te s-like states is approximately 84% in both c-CGT and a-CGT. The relative contributions of these anion s-like states are comparable to that in the typical covalent sp^3-bonded material, GaAs, of 89.9%. Contributions to this band from other states, principally from Ge s-like states, are less than 10%. The second deepest band, which peaks at 8.5 eV, is comprised mainly of Ge s-like states, which make up 52.7% and 56.1% of the band in c-GCT and a-GCT, respectively. Contributions from Te s and Te p states are 23.5% and 16.1%, respectively in c-CGT and are again comparable to the As s-like and p-like state contributions of 18.4% and 28.7% in the predominantly Ga s-like band of the GaAs spectrum [35]. The hybridization is weakened in a-CGT, as evidenced by a decrease in the contribution of Te s-like and p-like states to 14.9% and 7.8%, respectively.

In the crystalline phase, there is an increased participation of Te s and p electrons to the bonding network with the asymmetric sp^3 orbitals, whereas the geometry around the Cu atoms forces some of the electrons to form localized nonbonding d states. The loss of the long-range order in the amorphous phase allows the Te atoms to form lone-pair states, and the resulting weakening of the bonding network is compensated by the participation of the additional Cu d electrons in the bonding, in part by delocalization into empty Te d orbitals. This points to the key driver of the reversible PC being the tendency of the Te atoms to form lone-pair states, coupled with the structural flexibility afforded by the valence d shell of the Cu atoms. These together allow for the formation of a metastable amorphous phase.

Figure 3(b) shows the structure of a-CGT obtained by the *ab initio* molecular-dynamics melt-quench simulation in Ref. [32]. One of the most characteristic structural features of the model is that the bond-angle distribution (BAD) for Cu possesses a sharp peak at around 60°, indicating the presence of threefold ring configurations. These threefold rings predominantly occur in dense Cu-rich regions composed of Cu_3[Ge, Te] tetrahedra. This result is consistent with the electronic structure of the a-CGT phase discussed above. It is in keeping with Chen *et al.*'s recent DFT simulation of the electronic and structural aspects of the phase change in CGT [36], wherein it was reported that Te 5s electrons form localized lone-pair states in the amorphous phase, while Cu d states delocalize to form an extended charge density over the whole structure. The structure proposed from computational modeling is also consistent with experimental characterization of the local structure of a-CGT [37,38].

As discussed above, the PC in CGT is triggered by changes in the chemical bonding, which involve Cu and Te. These changes are essentially electronic transitions, and thus are faster than atomic movements in a diffusion process. The structural model of the amorphous phase that we obtained [Fig. 3(b)], however, indicates that Cu atoms tend to cluster by forming Cu-Cu metallic bonds, which are apparent as threefold ring units with the peaking of the BAD at 60° [32,36]. This suggests that the reconstruction of bonding around the Cu atoms inevitably involves a certain range of Cu atom movements to form Cu-Te-Ge bonding arrangements upon the PC. Consequently, the diffusion process of Cu atoms is considered to be a bottleneck for the reversibility and speed of the PC process. It is well known that Cu atoms can diffuse anomalously fast in elemental and compound semiconductors [39–53]. Ma and Wei have shown that Cu atoms, whose smallness allows their accommodation in interstitial sites without elastic-energy increases, can find energetically favorable diffusion paths due to a strong coupling between Cu 3d orbitals and host empty s orbitals caused by a lowering of the local symmetry from O_h or T_d symmetries [54]. In the a state, the Cu 3d-host s-orbital hybridization is expected to be more enhanced due to a lowering of the local symmetry; thus, Cu atoms can find energetically favorable sites more easily than in the c phase.

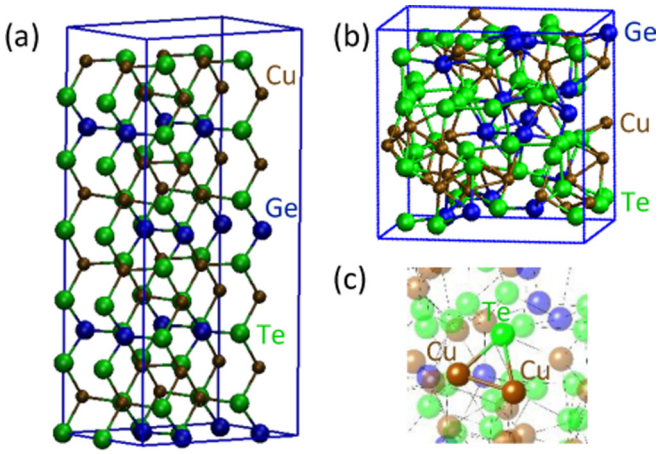

FIG. 3. The atomic arrangements for (a) crystalline and (b) amorphous phases. The color coding of the atoms is as follows: Cu, copper; Ge, blue; Te, green. (c) Zoom-in image of the amorphous phase highlighting a Cu threefold ring.

Together with the inherent tendencies in chemical bonding of Te and Cu, which cause the formation of a metastable amorphous phase, the fast diffusion of Cu atoms allows a relatively fast recrystallization by a reorganization of the electronic structure, to regenerate the crystalline bonding network.

The DOS calculation results indicate that no significant band gap widening occurs in the a-CGT phase compared to the c-CGT phase, as shown in Fig. 4. This is an essential difference to bear in mind in comparing the CGT family of alloys to the average-five-valence-electron ($\langle V \rangle$) family of materials, such as GST and AIST. For the case of the $\langle V \rangle$ family materials, the c-phase structure is theoretically of a metallic nature (although, in practice, ionicity and local structural distortions often yield a degenerate narrow-gap semiconductor) characterized by half-filled p-orbital resonance bonding of sixfold atoms. In the a phase, resonance bonding is broken upon quenching from the

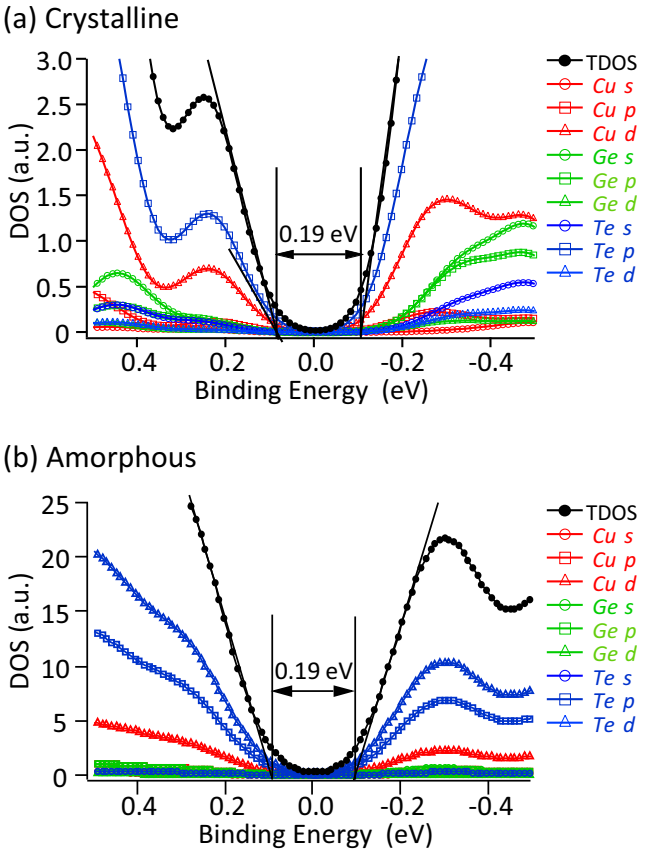

FIG. 4. Plots of PDOS and TDOS vs binding energy for: (a) crystalline; and (b) amorphous phases of CGT. Band gaps are almost the same for both phases.

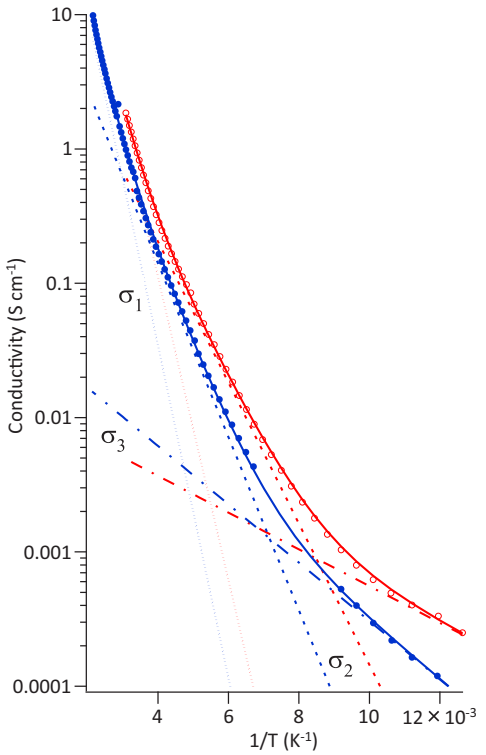

FIG. 5. Temperature dependence of conductivity data for two as-deposited CGT films plotted with fitting results (red and blue solid curves) using Eq. (1). Each exponential component in Eq. (1) is shown by red and blue dashed curves.

melt. The resultant amorphous structure is determined by one of the possible disordered structures in which the free energy is in a local minimum, determined by a balance between the gain of electronic free energy by widening the band gap and the loss due to increasing the elastic part of the free energy [18–20]. For GST225, the Fermi level is reported to be located in the middle of the widened band gap of 0.7 eV in the amorphous phase, thus it is considered to be an intrinsic semiconductor. On the other hand, in the crystalline phase, the Fermi level is located 0.17 eV above the top of the valence-band resulting in p-type conduction [18]. The thermal carrier concentration in the amorphous phase is determined by the distribution functions and the relevant DOS. The factor due to the distribution function in the amorphous phase is estimated as 1/10 of that in the crystalline phase. Assuming that the DOS in the tail states in the amorphous phase is about 1/10-1/100 of the valence-band DOS in the crystalline phase, the reduction of the thermal carrier density in the amorphous phase is estimated to be 10^{-3}. Considering that the mobility of the amorphous phase is expected to be about 10^{-3} smaller than that of the crystalline phase, the observed resistance contrast of 10^{-5}-10^{-6} between the two phases (see Fig. S1 in the Supplemental Material [33]) is reasonably explained by the band gap widening and changes in the density of states and the conduction mechanism in GST.

In the case of CGT, however, the valence instability that triggers the phase change is different. It is driven by the formation of Te 5s lone-pair states, which give rise to the delocalization of the Cu 3d electrons. In the experimental spectra, the Fermi level is positioned close to the top of the valence band in both phases. This means that the concentration of thermal carriers in CGT is not expected to change as drastically as in GST due to phase change. The optical-reflectivity change due to PC in CGT is smaller and has the opposite sign compared to that in GST, as previously reported [10].

An outstanding question regarding CGT is the origin of the orders-of-magnitude higher resistivity of the amorphous phase, which is, at first sight, unexpected in that it has a comparable band gap to the crystalline phase, as shown in Fig. 4. In order to answer this question, the temperature dependence of the conductivity of the as-deposited CGT amorphous film was measured by a four-point probe method in the van der Pauw geometry. As the value of the conductivity is generally structure sensitive, we measured two samples taken from different batches of the deposition to distinguish the process-independent properties from process-dependent properties. The surface of the film was capped with carbon layers to protect against oxidation in these measurements. There was no fluctuation of the resistance at around 200 °C, indicating that these film surfaces were not oxidized. The conductivity data show rapid monotonic increases as the temperature increases from 80–435 K. Figure 5 represents the measured conductivity as a function of inverse temperature for two different as-deposited amorphous films.

The temperature dependence of the conductivity can be successfully fitted by a sum of three different exponential

TABLE II. Fitting parameters for temperature dependences of the electrical conductivity of two as-deposited a-CGT films.

	σ_{01}(S cm^{-1})	E_1 (eV)	σ_{02}(S cm^{-1})	E_2 (eV)	σ_{03}(S cm^{-1})	E_3 (eV)
film 1	3600	0.22	26	0.10	0.013	0.027
film 2	3100	0.25	55	0.13	0.046	0.043

functions, according to:

$$\sigma = \sigma_1 + \sigma_2 + \sigma_3 = \sigma_{01}\exp(-E_1/k_BT) + \sigma_{02}\exp(-E_2/k_BT) + \sigma_{03}\exp(-E_3/k_BT). \quad (1)$$

Using this functional dependence, an excellent fit to the experimental data using a least-squares method was obtained with Δ values of 0.1% as shown in Fig. 5. If two exponential functions are used to fit the high- and low-temperature regions, or for the high- and mid-temperature regions, the fit is worse with Δ values of 3-4%. In this fitting procedure, we assume that the preexponential factors are temperature independent, despite that they should be functions of temperature, depending on the conduction mechanism [43–45]. We have confirmed that this neglect of the temperature dependence does not cause essential changes in the activation energies and quality of curve fitting compared with those values obtained using temperature-dependent preexponential factors. In order to distinguish the process-independent and dependent parameters, we performed the same fitting procedure on two samples taken from two deposition batches carried out using the same deposition conditions, as listed in Table II.

The fitting results can be very consistently understood by adopting the model for the conduction mechanism in disordered semiconductors proposed by Davis and Mott [55], which is based on a band structure schematically illustrated in Fig. 10(a). The model assumes a gap between filled and empty extended bands, and localized states, which tail from the filled valence and the empty conduction band into the gap, similar to the mobility-edge model of Cohen, Fritzsche, and Ovshinsky [56]. It further assumes a localized band of compensated levels due to defects, in which the Fermi level is pinned very near to the middle of the gap.

According to the Davis and Mott (DM) model, the first term in Eq. (1) represents conduction in the extended-state bands due to the thermal excitation of carriers. The activation energy is given by

$$E_1 = E_f\text{-}E_{mv},$$

where E_{mv} is the edge of the extended-state valence band [56–58]. We have confirmed the carrier type of both phases by Seebeck measurements and found that both showed p-type conduction as usually observed in typical phase-change materials. So, in this analysis, we are assuming that hole conduction dominates. The activation energies, E_1, for the two samples are 0.22 eV and 0.25 eV, as listed in Table II.

The second term is due to excitation of holes to E_B, representing a hopping conduction in the localized valence-band tail states. The activation energy is given by

$$E_2 = E_f\text{-}E_B + \Delta W.$$

The experimental activation energies are 0.10 eV and 0.13 eV for the two samples, as listed in Table II. The hopping energy ΔW is assumed to be a fraction of E_f-E_B [55]. Thus, E_B-E_{mv} is estimated to be less than E_1-$E_2 = 0.12$ eV.

The third term is due to conduction by hopping of carriers between filled and empty sites near the Fermi-level energy in the compensated defect band, and this is referred to as nearest-neighbor hopping (NNH). The activation energy gives a rough estimation of the half-width of the defect band [55]. The experimental activation energies of 0.027 and 0.043 eV in Table II seem to be reasonable for the defect-band half-width energy. Rather large differences in the activation energies among the samples are also reasonably understood since the defect band is considered to be strongly dependent on the film-fabrication procedure. On the other hand, we consider that differences in the film deposition conditions are not significant enough to result in detectable changes in the valence-band spectra.

Regarding the preexponential factors, the values of σ_{01} (3600 and 3100 S cm^{-1}) for the conduction of carriers in the extended band are comparable to typical values of σ_{01} for chalcogenide glasses [55,59]. The two samples had σ_{02}/σ_{01} ratios of 0.7×10^{-2} and 1.8×10^{-2} and σ_{03}/σ_{02} ratios of 5×10^{-4} and 8.4×10^{-4}, respectively; these values seem reasonable in that they are comparable to the ratios reported for other amorphous chalcogenide semiconductors for hopping conduction via tail states and the midgap defect band [55].

At very low temperatures, the hopping-conduction mode is expected to change to variable-range hopping (VRH), whose temperature dependence can be expressed as:

$$\sigma_4 = (A/T^{1/2})\exp(T_0/T^{-1/4}) \quad (2)$$

with $T_0 = 18a^3/k_BN_\mu$ and $A_3 = e^2\nu[N_\mu/32\pi k_Ba]^{1/2}$ [60]. Here, a is the inverse averaged hopping distance, k_B is the Boltzmann constant, N_μ is the density of trap states at the Fermi level, and ν is the phonon frequency, which serves as an attempt frequency [60,61]. Replacing the third term in Eq. (1) by Eq. (2), we obtained the same grade of quality in the fitting for both films. We assumed the relevant phonon frequency to be $\nu = 10^{13}$ s^{-1} with the resulting fitting parameters $d = 1/a$, and N_μ assuming values of 1.1×10^{-7} cm and 5.0×10^{19} cm^{-3} eV^{-1}, and 8.7×10^{-9} cm and 4.3×10^{22} cm^{-3} eV^{-1}, respectively, for the two films. The first set seems to be reasonable; however, the second set is less reasonable due to an unphysically short hopping distance, a distance less than the shortest bond length. This suggests that the temperature range of the present measurements is still not lower than the crossover temperature between the NNH- and VRH-conduction regimes.

Figure 6 shows spectral-density variations near the Fermi level due to annealing, as measured by the 5.4 keV Laboratory HXPES system. The onset of the spectrum is defined by the intersection of a linear extrapolation of the spectral edge and the background level. The onset stayed unchanged, and the occupation of the density of states at the Fermi level, $DOS(E_f)$,

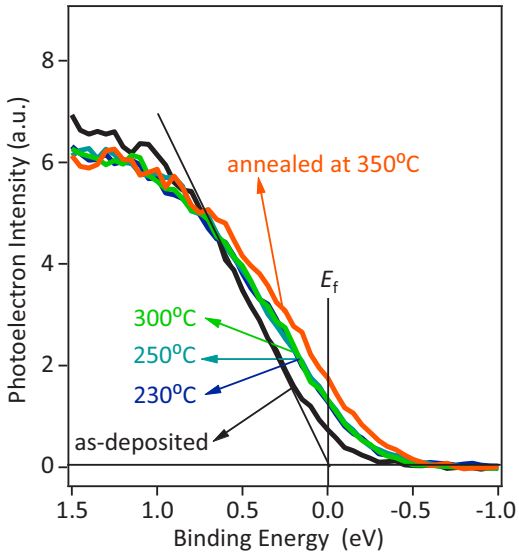

FIG. 6. Variation of valence-band edge spectra for as-deposited and annealed CGT films at different temperatures measured by a laboratory HXPES system with a monochromatic Cr Kα (5.4 keV) x-ray source.

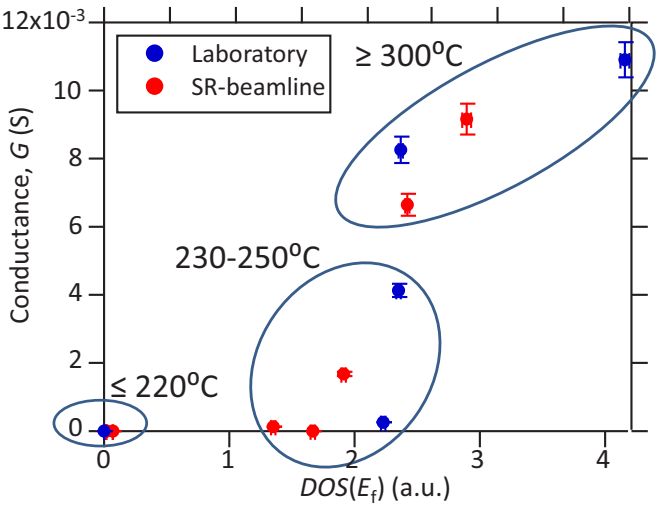

FIG. 7. Plot of G as a function of $DOS(E_f)$. In this figure, we superpose two plots using results of the two different $DOS(E_f)$ measurements obtained by the laboratory (blue) and the SR-beamline (red) HXPES apparatuses [62]. For the laboratory data, we subtracted an offset value from the $DOS(E_f)$ data, and then rescaled to produce coincidence between the $DOS(E_f)$ dependences for the two sets of data.

is negligibly small in the as-deposited films. The spectral edge shifts toward lower binding energies discontinuously on increasing the annealing temperature to 250 °C. The $DOS(E_f)$ also increases to a recognizable level in accordance with the edge shift. The edge stays at the same position for annealing up to 300 °C. For 350 °C annealing, the occupation at the Fermi level becomes clearer, exhibiting a weak metallic Fermi edge. The film can be considered to turn into a degenerate semiconductor.

In order to investigate these variations of spectral shape near the Fermi level in more detail, we have recently performed valence-band measurements at BL47XU at SPring-8 using excitation with undulator x rays at 8 keV [62]. The evolution of the spectral shape with increasing annealing temperature near the Fermi level is reproduced with a higher resolution, as shown in Fig. S2 in the Supplemental Material [63]. These results confirm that the spectral onset stays at the same position of 0.145 eV below the Fermi level when the annealing temperature is below 220 °C. When the annealing temperature exceeds 235 °C, the spectrum shows a shoulder structure, which is superposed onto the linear extrapolation of the spectral edge. As a result, the onset discontinuously shifts toward a lower binding energy to touch the Fermi level. The spectral feature is still stable when the annealing temperature reaches 250 °C. When the annealing temperature exceeds 300 °C, the spectral shape again shows discontinuous changes. The shoulder structure disappears and a finite hole occupation is recognized at the Fermi level. The hole occupation further increases when the annealing temperature increases to 350 °C.

Combining the laboratory HXPES data and the new synchrotron radiation (SR) HXPES results, we determined the conductance G vs $DOS(E_f)$, as shown in Fig. 7. In this figure, we superpose the two plots, using the results of the two different $DOS(E_f)$ measurements, that is, the data obtained by the laboratory system (blue) and the data obtained from synchrotron-based measurements (red) [62] (see Fig. S3 in the Supplemental Material [64]). For the laboratory data, we integrated the photoelectron signal intensity in the region 0.5 eV on either side of the Fermi level to estimate the occupied carrier density of states at the Fermi level, i.e., $DOS(E_f)$. On the other hand, the higher energy resolution and larger signal intensity of the synchrotron measurements enabled us to determine the $DOS(E_f)$ without integration. The above difference in resolution results in an artifact (offset) in the comparison of the $DOS(E_f)$ derived from the laboratory HXPES and that determined from the synchrotron HXPES. This offset was subtracted from the laboratory data so that the two $DOS(E_f)$ would have the same origin. Subsequently, we rescaled the $DOS(E_f)$ axis by the ratio of the DOS values for the films annealed at 250 °C. The resulting G vs $DOS(E_f)$ plots for the two sets of the data are in good agreement as can be seen in Fig. 7.

The annealing process is divided into three stages, as depicted in Fig. 7. In the first stage, where the annealing temperature does not exceed 220 °C, the films show essentially no change in electronic structure and transport properties. In the second stage, at an annealing temperature between 220 and 230 °C, the film conductivity discontinuously increases and continues to increase with increasing annealing temperature up to 250 °C. However, it stays significantly lower than the values for G in the final stage. Crystallization of the film was evident in x-ray diffraction data at an annealing temperature of 232 °C. Indeed, transmission-electron-microscope observations indicate that the 230 °C annealed films contain crystalline grains, as shown in Fig. 8. Electron-beam-diffraction measurements clarified that crystalline diffraction patterns are obtained regardless of the position of the observation area over the field of view. This indicates that percolation, which in this case means the point when crystal grains touch each other continuously

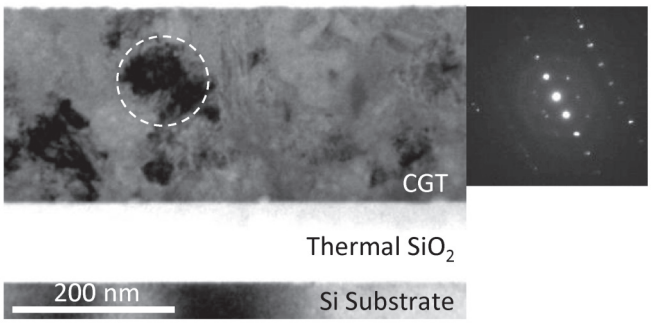

FIG. 8. Cross-sectional bright-field TEM image of a CGT film annealed to 232 °C. The right-top figure shows a selected-area diffraction pattern (SADP) taken from the white dotted circle in the TEM image. Although grain boundaries are not clearly observed in the bright-field image, the SADP shows a small number of spots aligned in a particular direction instead of a ring pattern, indicating that there are only a few grains in the area being examined. The grain size can be roughly estimated to be about 100 nm. The small number of diffraction spots observed in the SADPs was repeated for numerous locations throughout the film, revealing that the crystallization proceeds appreciably.

throughout the film, has been completed in this stage. In the third stage, where the annealing temperature exceeds 300 °C, the finite DOS at E_f and high conductance values suggest that the crystallized films are turned into degenerate semiconductors in this annealing stage.

Figure 9(a) shows a conductance vs inverse temperature plot of the film conductance after crystallization for different annealing temperatures. It is clear that the temperature coefficient of the resistance changes from being negative to positive at a critical temperature T_c between annealing temperatures of 250 and 300 °C. In other words, the conduction in the films after annealing at a temperature between 230 °C and T_c is not metallic due to remaining randomness, even after crystallization is completed. Similar behavior has been observed in the temperature dependence of the resistivity in the typical phase-change material, GST [65]. The remaining disorder in the GST crystalline state, just after the crystallization, results in a mobility edge, E_μ, below E_f, resulting in a semiconductor-like negative temperature coefficient of the resistivity [65]. Figure 9(b) and 9(c) show log G vs $1/T$ plots for films taken after 230 and 250 °C annealing, respectively, that have been fit using two exponential functions. The fitting error Δ was 3.4%, and 0.5% for 230 and 250 °C annealed films, respectively. The temperature dependence of the conductance of the films is composed of two exponential components, with activation energies of 183 meV and 5.6 meV, and 140 meV and 4.3 meV, respectively. It is reasonable to assume that the larger value corresponds to the activation energy that is necessary for hole excitation in extended states, and the smaller one to the activation energy for hopping conduction in the tail states. In both films, hopping in the tail states dominates the conductance at room temperature. The conductance, G, shows a moderate increase when the annealing temperature is raised to 300-350 °C, as seen in Fig. 7. All the results mentioned above indicate that there are three stages in the course of the annealing.

This three-stage behavior of the annealing process is reasonably explained by the same DM model that we adopt to explain the temperature dependence of the conductivity of the as-deposited films. As shown schematically in Fig. 10(a), the Fermi-level position is stably pinned in the defect band in the band gap in stage 1. The conduction at room temperature is dominated by thermal excitation of the carriers into the extended valence- and conduction-band states across the mobility gap (σ_1). In stage 2 [Fig. 10(b)], crystalline grains appear and eventually percolate through the whole film. The defect bands, which cause the Fermi-level pinning, are already annealed out. The Fermi level discontinuously jumps into the tail states of the valence band. Conduction is dominated by the hopping of carriers in tail states, where carriers are trapped by the random potential and thus the conductivity is still low and the temperature coefficient of resistivity is still negative. In stage 3 [Fig. 10(c)], crystalline order in the grains recovers and the tail states disappear. As the traps are annihilated by annealing, carriers are released, and thus the films transform into degenerate semiconductors, showing a positive temperature coefficient of resistivity.

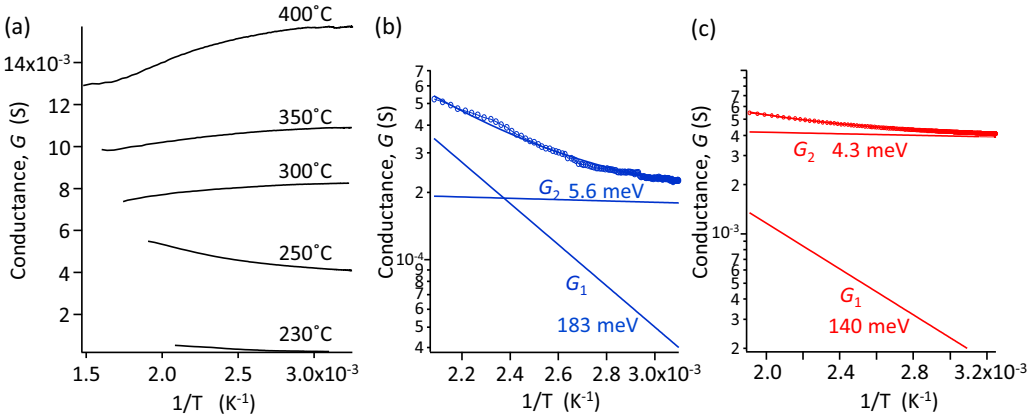

FIG. 9. (a) Conductance, G, for annealed films as a function of temperature, where a two-point probe method was used for the measurement. Note that the sign of the temperature dependence changes at an annealing temperature between 230 and 250 °C. (b) log G vs $1/T$ plot for a film annealed at 230 °C. (c) The same for a film annealed at 250 °C.

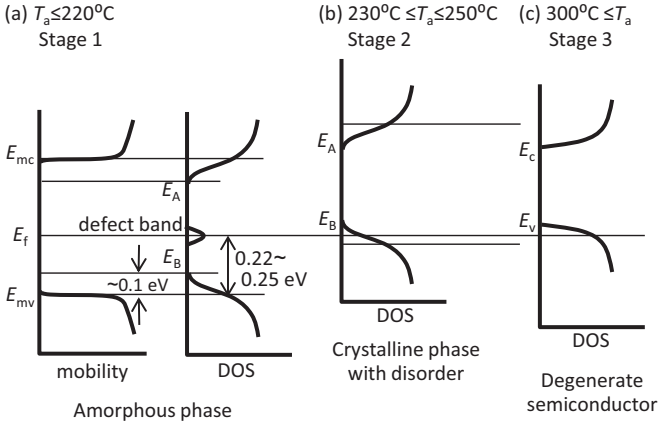

FIG. 10. Schematic diagram of three-stage band-structure changes during the phase change in CGT.

Although percolation of the crystalline grains is already finished in stage 2, as seen in Fig. 8, there is a possibility that grain boundaries control the conduction. If we assume that, inside the grains, the material behaves as a crystalline degenerate semiconductor and the barriers are at the grain boundaries, then the temperature coefficient of conductance should be positive. However, this should result in the appearance of a metallic edge in the photoelectron spectra, the same as that observed in stage 3. Apparently this is not the case in the present experimental results.

IV. CONCLUSIONS

Summarizing the present results, we have measured the evolution of the HXPES valence-band spectra and electrical-transport properties of CGT during the annealing process from the as-deposited amorphous phase to the crystalline phase. The valence-band spectra in both crystalline and amorphous phases are well reproduced by the calculated partial densities of states obtained from hybrid DFT calculations. The combination of theory and experiment has yielded a consistent model for the PC mechanism in which Te 5*s* lone-pair formation in the amorphous phase induces the enhanced participation of Cu 3*d* states in the bonding in an interaction with the empty Te 4*d* orbitals. In addition to the above-mentioned rapid reversible bond-reconstruction mechanism, anomalously fast diffusion of Cu atoms in the amorphous matrix is likely to be another key to the fast PC switching. The temperature dependence of the conductivity in as-deposited films is well reproduced by three exponential components, adopting the Davis-Mott (DM) model proposed for disordered semiconductors. That is, the conductivity is determined by a superposition of interband thermal excitation of carriers in the extended bands, hopping conduction in valence-band tail states, and hopping conduction in a defect band near the middle of the band gap. At room temperature, the conduction is predominantly in the extended states, which involves an activation energy of 0.22-0.25 eV. The annealing behavior of the transport and spectroscopic data are consistently analyzed on the basis of the same D-M model. The midgap defect band, which pins the Fermi level, is annealed out at around 230 °C, resulting in a discontinuous shift of the Fermi level to near the valence-band maximum. The transport channel is changed from conduction in the extended states in the amorphous phase to metallic conduction in a crystalline degenerate semiconductor via hopping conduction in disorder-induced tail states in the defective crystalline semiconductor. The high resistance in the *a* phase, which provides a clear contrast with the low resistance in the *c* phase, is due to the Fermi-level pinning in the *a* phase at the midgap defect band. This suggests that the robustness of the defect band against temperature stress is a key to achieving practical device applications.

ACKNOWLEDGMENTS

This work was supported by KAKENHI (Grant No. 15H04113) and the Kato Foundation for Promotion of Science. J.M.S. is grateful for the support of an Internal Graduate Studentship award from Trinity College, Cambridge, and for funding from the UK Engineering and Physical Sciences Research Council (EPSRC, Grant No. EP/K004956/1). The calculations were performed using the UK Archer HPC facility, accessed through the UK Materials Chemistry Consortium (MCC), which is funded by the EPSRC (Grant No. EP/L000202). A subset of the calculations was also performed on the Balena HPC facility at the University of Bath, which is maintained by Bath University Computing Services. Y.S. and S.S. acknowledge Prof. Junichi Koike for valuable discussions.

[1] G. W. Burr, M. J. Breitwisch, M. Franceschini, D. Garetto, K. Gopalakrishnan, B. Jackson, B. Kurdi, C. Lam, L. A. Lastras, A. Padilla *et al.*, J. Vac. Sci. Technol. B **28**, 223 (2010).
[2] M. Wuttig, Nature Mater. **4**, 265 (2005).
[3] M. Wuttig and N. Yamada, Nature Mater. **6**, 824 (2007).
[4] M. Zhu, M. Xia, F. Rao, X. Li, L. Wu, X. Ji, S. Lv, Z. Song, S. Feng, H. Sun *et al.*, Nat. Commun. **5**, 4086 (2014).
[5] N. Yamada, E. Ohno, K. Nishiuchi, N. Akahira, and M. Takao, J. Appl. Phys. **69**, 2849 (1991).
[6] H. Iwasaki, Y. Ide, M. Harigaya, Y. Kageyama, and I. Fujimura, Jpn. J. Appl. Phys. Part 1 **31**, 461 (1992).
[7] S. Raoux, R. M. Shelby, J. Jordan-Sweet, B. Munoz, M. Salinga, Y. C. Chen, Y. H. Shih, E. K. Lai, and M. H. Lee, Microelectron. Eng. **85**, 2330 (2008).
[8] Y. Sutou, T. Kamada, M. Sumiya, Y. Saito, and J. Koike, Acta Mater. **60**, 872 (2012).
[9] T. Kamada, Y. Sutou, M. Sumiya, Y. Saito, and J. Koike, Thin Solid Films **520**, 4389 (2012).
[10] Y. Saito, Y. Sutou, and J. Koike, Appl. Phys. Lett. **102**, 051910 (2012).
[11] Y. Saito, Y. Sutou, and J. Koike, J. Phys. Chem. C **118**, 26973 (2014).
[12] G. Lucovsky and P. M. White, Phys. Rev. B **8**660 (1973).

[13] K. A. Khachaturyan, Phys. Rev. B **36**, 4222 (1987).
[14] K. L. I. Kobayashi *et al.*, Prog. Crystal Growth and Charact. **1**, 117 (1978).
[15] T. Suski, J. Karpinski, K. L. I. Kobayashi, and K. F. Komatsubara, J. Phys. Chem. Solids **42**, 479 (1981).
[16] P. B. Littlewood, J. Phys. C: Solid State Phys. **13**, 4855 (1980).
[17] K. Shportko, S. Kremers, M. Woda, D. Lencer, J. Robertson, and M. Wuttig, Nature Mater. **7**, 653 (2008).
[18] J. J. Kim, K. Kobayashi, E. Ikenaga, M. Kobata, S. Ueda, T. Matsunaga, K. Kifune, R. Kojima, and N. Yamada, Phys. Rev. B **76**, 115124 (2007).
[19] J. Akola, R. O. Jones, S. Kohara, S. Kimura, K. Kobayashi, M. Takata, T. Matsunaga, R. Kojima, and N. Yamada, Phys. Rev. B **80**, 020201(R) (2009).
[20] T. Matsunaga, J. Akola, S. Kohara, T. Honma, K. Kobayashi, E. Ikenaga, R. O. Jones, N. Yamada, M. Takata, and R. Kojima, Nature Mater. **10**, 129 (2011).
[21] G. E. Delgado, A. J. Mora, M. Pirela, A. Velasquez-Velasquez, M. Villarreal, and B. J. Fernandez, Phys. Status Solidi A **201**, 2900 (2004).
[22] K. Kobayashi, Appl. Phys. Lett. **83**, 1005 (2003).
[23] K. Kobayashi, Nucl. Instr. Meth. Phys. Res. A **547**, 98 (2005).
[24] K. Kobayashi, Nucl. Instr. Meth. Phys. Res. A **601**, 32 (2009).
[25] M. Kobata, I. Igor, H. Iwai, H. Yamazui, H. Takahashi, M. Suzuki, H. Matsuda, H. Daimon, and K. Kobayashi, Anal. Sci. **26**, 227 (2010).
[26] K. Kobayashi, M. Kobata, and H. Iwai, J. Elec. Spectr. Rel. Phenom. **190**, 210 (2013).
[27] G. Kresse and J. Hafner, Phys. Rev. B **47**, 558 (1993).
[28] Y. Saito, S. Shindo, Y. Sutou, and J. Koike, J. Phys. D: Appl. Phys. **47**, 475302 (2014).
[29] P. E. Blochl, Phys. Rev. B **50**, 17953 (1994).
[30] C. Adamo and V. Barone, J. Chem. Phys. **110**, 6158 (1999).
[31] H. J. Monkhorst and J. D. Pack, Phys. Rev. B **13**, 5188 (1976).
[32] J. M. Skelton, K. Kobayashi, Y. Sutou, and S. R. Elliott, Appl. Phys. Lett. **102**, 224105 (2013).
[33] See Supplemental Material at http://link.aps.org/supplemental/10.1103/PhysRevB.97.195105 for details on the temperature dependence of resistance for GST225 and CGT films.
[34] M. B. Trzhaskovskaya, V. K. Nikulin, V. I. Nefedov, and V. G. Yarzhemsky, At. Data Nucl. Data Tables **92**, 245 (2006).
[35] LDA calculations by T. Yamamoto (private communication).
[36] N. K. Chen, X. B. Li, X. R. Wang, M. J. Xia, S. Y. Xie, H. Wang, Z. Song, S. Zhang, and H. B. Suna, Acta Mater. **90**, 88 (2015).
[37] P. Jóvári, Y. Sutou, I. Kaban, Y. Saito, and J. Koike, Scripta Mater. **68**, 122 (2013).
[38] K. Kamimura, S. Hosokawa, N. Happo, H. Ikemoto, Y. Sutou, S. Shindo, Y. Saito, and J. Koike, J. Optoelectron. Adv. Mater. **18**, 248 (2016).
[39] R. N. Hall and J. H. Racette, J. Appl. Phys. **35**, 379 (1964).
[40] M. B. Dutt and B. L. Sharma, *Landolt-Börnstein - Group III Condensed Matter, 33A, Diffusion in Semiconductors and Non-Metallic Solids, 3 Diffusion in compound Semiconductor* (Springer-Verlag, Berlin, 1998).
[41] J. D. Struthers, J. Appl. Phys. **27**, 1560 (1956).
[42] A. A. Istratov, C. Flink, H. Hieslmair, E. R. Weber, and T. Heiser, Phys. Rev. Lett. **81**, 1243 (1998).
[43] C. S. Fuller and J. D. Struthers, Phys. Rev. **93**, 1182 (1954).
[44] C. S. Fuller and J. M. Whelan, J. Phys. Chem. Solids **6**, 173 (1958).
[45] C. Hilsum, Proc. Phys. Soc. London **73**, 685 (1959).
[46] H. J. Stocker, Phys. Rev. **130**, 2160 (1963).
[47] R. H. Wieber, H. C. Gorton, and C. S. Peet, J. Appl. Phys. **31**, 608 (1960).
[48] R. L. Clarke, J. Appl. Phys. **30**, 957 (1959).
[49] E. D. Jones and J. C. Clark, in *Diffusion of Group I, II, and III Impurities in CdTe*, edited by P. Capper, Properties of Narrow Gap Cadmium based Compounds, EMIS Data Reviews (INSPEC, London, 1994).
[50] E. D. Jones, N. M. Stewart, and J. B. Mullin, J. Cryst. Growth **117**, 244 (1992).
[51] H. H. Woodbury and M. Aven, J. Appl. Phys. **39**, 5485 (1968).
[52] T. Lukaszewicz, Phys. Status Solidi A **73**, 611 (1982).
[53] T. Lukaszewicz and J. Zmija, Phys. Status Solidi(a) **62**, 695 (1980).
[54] J. Ma and S. H. Wei, Phys. Rev. Lett. **110**, 235901 (2013)
[55] E. A. Davis and N. F. Mott, Phil. Mag. **22**, 0903 (1970)
[56] M. H. Cohen, H. Fritzsche, and S. R. Ovshinsky, Phys. Rev. Lett. **22**, 1065 (1969).
[57] P. W. Anderson, Phys. Rev. **109**, 1492 (1958).
[58] N. F. Mott, Phys. Today **31**(11), 42 (1978).
[59] F. Skuban, S. R. Luki, D. M. Petrovi, I. Savi, and Yu. S. Tver'yanovich, J. Optoelectron. Adv. Mater **7**, 1793 (2005).
[60] N. F. Mott, J. Non-Cryst. Solids **1**, 1 (1968).
[61] B. I. Shklovskii and A. L. Efros, *Electronic Properties of Doped Semiconductors* (Springer-Verlag, Berlin, 1984).
[62] Y. Saito, Y. Sutou, P. Fons, S. Shindo, X. Kozina, J. M. Skelton, A. V. Kolobov, and K. Kobayashi, Chem. Mater. **29**, 7440 (2017).
[63] See Supplemental Material at http://link.aps.org/supplemental/10.1103/PhysRevB.97.195105 for details on the high-resolution variation of valence-band edge spectra for as-deposited and annealed CGT films.
[64] See Supplemental Material at http://link.aps.org/supplemental/10.1103/PhysRevB.97.195105 for details on the annealing temperature dependences of electrical conductance and density of states at the Fermi level of CGT films.
[65] T. Siegrist, P. Jost, H. Volker, M. Woda, P. Merkelbach, C. Schlockermann, and M. Wuttig, Nature Mater. **10**, 202 (2011).